PCCP

Accepted Manuscript

ROYAL SOCIETY OF CHEMISTRY

www.rsc.org/pccp

Journal Name

RSCPublishing

ARTICLE

Analysis of parahydrogen polarized spin system in low magnetic fields

Cite this: DOI: 10.1039/x0xx00000x

P. Türschmann[a,b], J. Colell[a], T. Theis[c], B. Blümich[a], and S. Appelt[a,d]

Received ooth January 2012,
Accepted ooth January 2012

DOI: 10.1039/x0xx00000x

www.rsc.org/

Nuclear magnetic resonance (NMR) spectra of spin systems polarized either thermally or by parahydrogen exhibit strikingly different field dependencies. Thermally polarized spin systems show the well-known roof effect, observed when reducing magnetic field strengths which precludes the independent determination of chemical shift differences and *J*-coupling constants at low-fields. Quantum mechanical analysis of the NMR spectra with respect to polarization method, pulsed state preparation, and transition probabilities reveals that spectra of parahydrogen polarized systems feature an "inverse roof effect" in the regime where the chemical shift difference δυ is smaller than *J*. This inverse roof effect allows for the extraction of both *J*-coupling and chemical shift information down to very low fields. Based on a two-spin system, the observed non-linear magnetic field dependence of the splitting of spectral lines is predicted. We develop a general solution for the steady state density matrix of a parahydrogen polarized three-spin system including a heteronucleus which allows explaining experimentally observed ^{1}H spectra. The analysis of three-spin density matrix illustrates two pathways for an efficient polarization transfer from parahydrogen to ^{13}C nuclei. Examination of the experimental data facilitates the extraction of all relevant NMR parameters using single-scan, high-resolution ^{1}H and ^{13}C NMR spectroscopy at low fields at a fraction of the cost associated with cryogenically cooled high-field NMR spectrometers.

1. Introduction

NMR with thermally polarized spin ensembles is inherently insensitive because the population differences of nuclear Zeeman levels are small at room temperature even in strong magnetic fields of several Tesla. This problem can be overcome by coupling nuclear spins to a reservoir with higher state purity. Examples include circularly polarized light used in spin-exchange optical pumping (SEOP), polarized electron spins at low temperatures and large magnetic fields (DNP) or the anti-symmetric singlet state of parahydrogen (Parahydrogen Induced Polarization, PHIP) [1-5]. The development of hyperpolarization methods, in which the source of the polarization is not the magnetic field B_0, has contributed to a new trend - the exploration of NMR at low-magnetic fields. In contrast to the increasing acquisition and operating expenses associated with increasing magnetic field strengths low field NMR technology is affordable and requires nearly no maintenance. Especially, the combination of hyperpolarization with alternative and highly sensitive detection schemes like super-conducting quantum interference devices (SQUIDs), atomic-magnetometers, and nitrogen-vacancy centres has extended the scope of low-field magnetic resonance spectroscopy and imaging to ultra-precise spectral and spatial resolutions [6-13]. These developments are driven by the prospect of low-cost portable NMR spectrometers which could be made broadly available. In this contribution we describe inductively detected low-field NMR experiments which retain the critical NMR parameters used for structure elucidation: *J*-coupling and chemical shift. In low-magnetic fields of a few mT, as used in our experiments, the chemical shift-difference $\delta\upsilon$ between two spins at different positions in a molecule is small compared to the electron mediated dipole-dipole interaction, the *J*-coupling [13,14]. Thus, spin systems at low-fields are typically deemed "strongly coupled systems". Normally, strongly coupled spin systems inhibit the determination of *J*-coupling and chemical shift difference from thermally polarized ensembles. However, our recent experiments show that this no longer holds for parahydrogen hyperpolarized spin systems [16] where PHIP enables a pure spin state initialization independent of the external magnetic field [17]. Expanding these ideas, the detection and manipulation of single spins and hyperpolarized spin systems opens many additional applications of nuclear magnetic resonance ranging from biomolecular imaging to quantum computation [18-22]. Additional

interest in PHIP at low magnetic fields is constituted by the fact that polarization stored in singlet states on pairs of strongly coupled spins can be long lived with population lifetimes exceeding minutes and coherence times in the order of tens of seconds [23,24]. A fundamental understanding of entangled spin systems and their decoherence mechanisms is therefore of general interest.

In section two, we present the quantum mechanical description of a homonuclear *J*-coupled two-spin system I_1I_2 and a heteronuclear *J*-coupled three-spin system I_1I_2S, both starting from thermal and parahydrogen induced polarization. In section three a detailed analysis of the dipole transition moments is given to explain the phenomena denoted as roof effect and inverse roof effect for I_1I_2 systems [16, 25]. Most importantly, the relative amplitudes ratios observed in PHIP experiments show an inverted field dependence compared to spectra of thermally polarized spin systems. It is this phenomenon which allows for simultaneous determination of the chemical shift and *J*-coupling information in PHIP experiments conducted in the inverse weak coupling regime ($\delta\upsilon < J$) [16]. A theoretical evaluation of the amplitudes, expressed as signal-to-noise ratio (*SNR*), as a function of the external magnetic field elucidates the striking differences between the two polarization methods. Section four examines the field dependence of polarization transfer from the singlet order of hydrogen to a heteronucleus. Subsequently, the introduced models are compared with experimental spectra of two- and three-spin systems in the inverse weak coupling regime in section five. Furthermore, we discuss ^{13}C and ^{1}H spectra of PHIP hyperpolarized spin systems with more than three *J*-coupled spins. The high complexity of the measured spectrum of phenyl acetylene, for example, gives rise to the question what spectral information can be obtained from *n*-spin systems ($n > 3$). Lastly, details about the analytical calculations are provided in appendices A-D.

2. Thermal and parahydrogen induced polarization

In order to obtain a detectable NMR signal a spin system is typically polarized and subsequently subjected to a radio-frequency (rf) pulse described by a Hamiltonian of the form

$$\mathcal{H}_{rf} = \hbar B_1 \sum_i \gamma_i I_{ix} , \qquad (1)$$

where $\hbar$ is Planck's constant, γ_i is the gyromagnetic ratio of the *i*-th spin, B_1 is the resonant magnetic field strength of the rf-wave and I_{ix} is the *x*-component of the spin vector operators $\boldsymbol{I_i}$. The pulse angle $\Theta = \gamma_I B_1 \tau$ can be controlled via the pulse duration τ or amplitude B_1. Under the influence of $\mathcal{H}_{rf}$ the initial state of the density matrix ρ_0 evolves into ρ^θ. The intrinsic interaction Hamiltonian $\mathcal{H}_0$ causes further evolution of the density matrix. In general the Hamiltonian of a *J*-coupled spin system in a static external magnetic field, B_0, is defined as

$$\mathcal{H}_0 = \hbar B_0 \sum_i \gamma_i (1+\delta_i) I_{iz} + \sum_{i\neq j,\ i<j} J_{ij}\, \boldsymbol{I_i}\cdot\boldsymbol{I_j}. \qquad (2)$$

B_0 establishes the z-quantization axis, δ_i is the chemical shift of the *i*-th spin. The spins I_i and I_j are coupled by the scalar constant J_{ij}. $\boldsymbol{I_i}$ and $\boldsymbol{I_j}$ are the spin vector operators of the corresponding nuclei. The evolution of the prepared state under the intrinsic Hamiltonian $\mathcal{H}_0$ is detected in terms of the time dependent expectation value of the detection operator $\mathcal{D}$ (typically I_x, I_y or I_x+iI_y) defined as free induction $\langle \mathcal{D}(t) \rangle$.

$$\mathbf{Tr}\left[\boldsymbol{D}\, e^{-\frac{i}{\hbar}\mathcal{H}_0 t}\, e^{-\frac{i}{\hbar}\mathcal{H}_{\mathrm{rf}}\tau}\, \boldsymbol{\rho_0}\, e^{\frac{i}{\hbar}\mathcal{H}_{\mathrm{rf}}\tau}\, e^{\frac{i}{\hbar}\mathcal{H}_0 t}\right] \qquad (3)$$

The Fourier transform of expression (3) yields the NMR spectrum with infinitely small line widths, since decoherence effects are neglected. Experimentally, the observed resonances are associated with characteristic transverse relaxation times T_2 resulting in a decay of the free induction (FID) and finite linewidths.

2.1 Thermal polarization

As described in introductory NMR textbooks [25, 26] the diagonal elements of the density matrix in the Zeeman basis are populated according to the Boltzmann distribution if samples are thermally polarized. In the high temperature approximation, where the thermal energy k_BT is assumed to be larger than the energy of the Zeeman splitting $\hbar B_0 \gamma_I$, the density matrix ρ_B for a thermally polarized *n*-spin system is approximated by

$$\rho_B \approx \frac{1}{2^n}\left(\mathbb{E} + \beta \sum_i^n I_{iz}\right) \text{ with } \beta = \frac{\hbar B_0 \gamma_I}{k_B T}, \qquad (4)$$

where $\mathbb{E}$ is the $2^n \times 2^n$ dimensional unity matrix. The signal strength is proportional to β, where β is on the order of 10^{-5} even for nuclei with large γ at magnetic fields strengths of several Tesla. This results in low nuclear spin polarization and low *SNR*. Usally, a π/2 pulse is applied to the initial density matrix creating transverse magnetization. In these experiments the detected resonances appear in-phase. This is in contrast to experiments with parahydrogen polarization, where coherences can be phase shifted with respect to each other.

2.2. Parahydrogen induced polarization of a homonuclear two-spin I_1I_2 and heteronuclear I_1I_2S system

The nuclear spin state of a parahydrogen molecule is the singlet state $|S_0\rangle$ and the corresponding initial density matrix ρ_p on spins I_1 and I_2 is given as

$$\rho_p = |S_0\rangle\langle S_0| = \frac{1}{4}\mathbb{E} - \boldsymbol{I_1}\cdot\boldsymbol{I_2} = \frac{1}{4}\mathbb{E} - I_{1z}I_{2z} - ZQ_x \qquad (5)$$

with zero quantum coherence $ZQ_x = I_{1x}I_{2x} + I_{1y}I_{2y}$. The singlet state is an eigenstate of the *J*-coupling Hamiltonian $\mathcal{H}_J = 2\pi J_{12} \boldsymbol{I_1}\cdot\boldsymbol{I_2}$ but if the symmetry of spins I_1 and I_2 is broken by an intrinsic Hamiltonian $\mathcal{H}_0$ with a non-zero chemical shift difference in the form of Eq. (2), the singlet state is no longer an eigenstate and a detectable magnetization can be generated. Experimentally, a chemical-shift difference is established by addition of parahydrogen to an unsaturated bond in a way that the symmetry between both parahydrogen derived protons is removed in the reaction product. Explicitly, for a *J*-coupled spin system of two like spins I_1I_2 the intrinsic Hamiltonian is

$$\mathcal{H}^{I_1I_2} = \hbar\,(\omega_{1z}\, I_{1z} + \omega_{2z}\, I_{2z}) + 2\pi\, J_{12}\ \boldsymbol{I_1}\cdot\boldsymbol{I_2}, \qquad (6)$$

where $\upsilon_{iz} = \omega_{iz}/2\pi = \gamma_I B_0(1+\delta_i), i = 1,2$ are the Larmor frequencies of spins I_i separated by their chemical shift difference $\delta\upsilon = \gamma_I B_0(\delta_2 - \delta_1)$. For a two-spin system it is convenient to define the dimensionless parameter $x = \delta\upsilon/J_{12}$ whose magnitude defines the following three regimes: the weak coupling regime ($x \gg 1$) which is typically encountered at large magnetic fields, the strong coupling regime ($x \approx 1$), and the inverse weak coupling regime ($x \ll 1$) encountered typically at mT fields [27]. To encompass the effect of many hydrogenation reactions, occurring over time (for several seconds) on the statistical ensemble, a time averaged projection of the singlet state onto the product Hamiltonian $\mathcal{H}^{I_1I_2}$ from Eq. (6) gives the new populations. We refer to the result

as the incoherently averaged initial density matrix of PHIP, $\overline{\rho_p}$ [17]. Note that in Eq. (7) we just consider terms not proportional to the identity operator $\mathbb{E}$.

$$\overline{\rho_p} = I_{1z}I_{2z} + \frac{1}{1+x^2}ZQ_x + \frac{x}{2(x^2+1)}(I_{1z} - I_{2z}) \qquad (7)$$

Alternatively, the symmetry of the initial singlet state can be broken by *J*-coupling to a third spin (or more). In order to elucidate the fundamental mechanisms we introduce a third spin *S*=1/2 coupled differently to the protons initially in the singlet state, and thus creating a heteronuclear three-spin system I_1I_2S [28, 29]. The Hamiltonian $\mathcal{H}^{I_1I_2S}$ describes the interaction between the spins of this three-spin system consisting of two like spins I_1 and I_2 with similar Larmor frequency $\omega_{I1} \approx \omega_{I2}$ and a different spin species *S* with resonance frequency $\omega_S \neq \omega_I$. In both high and low magnetic fields of a few mT it is a valid approximation to consider just the *z*-component of heteronuclear *J*-coupling terms ($J_{1S}I_{1z}S_z$ and $J_{2S}I_{2z}S_z$). Note that near zero-field (μT) this approximation is no longer valid, as the Larmor frequency difference $\omega_S - \omega_I$ becomes comparable to the heteronuclear *J*-coupling constant [14]. In the mT regime the chemical shift difference between like spins I_1 and I_2 is typically < 1 Hz and can thus be either comparable to or smaller than their *J*-coupling constant J_{12} which means that all spin components have to be taken into account.

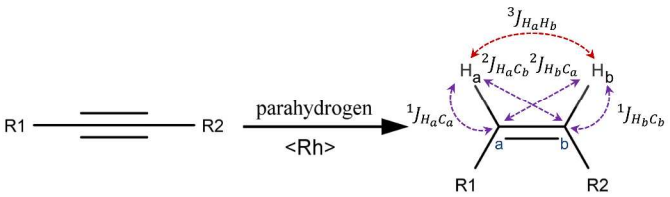

Fig. 1: Transition metal mediated chemical reaction of parahydrogen and a disubstituted ethyne molecule forming a hyperpolarized pseudo two-spin system in (*z*)-configuration after reduction. $^3J_{H_aH_b}$ is the homonuclear coupling constant. A naturally abundant heteronucleus, e.g. ^{13}C, either in position a or b couples differently to protons H_a and H_b with the coupling constants $^1J_{H_aC_a} \neq {}^2J_{H_aC_b}$ or $^2J_{H_bC_a} \neq {}^1J_{H_bC_b}$.

Figure 1 shows a ^{1}H two-spin system originating from hydrogenation of a disubstituted (R_1, R_2) ethyne molecule. The introduced protons can couple differently to an adjacent ^{13}C nucleus, establishing the following Hamiltonian acting on the created three-spin system.

$$\mathcal{H}^{I_1I_2S} = \hbar(\omega_{I1}I_{1z} + \omega_{I2}I_{2z} + \omega_S S_z) + 2\pi J_{12}\,\boldsymbol{I_1}\cdot\boldsymbol{I_2} + 2\pi J_{1S}\,I_{1z}S_z + 2\pi J_{2S}\,I_{2z}S_z \qquad (8)$$

The resulting time averaged projection of the singlet state under the influence of $\mathcal{H}^{I_1I_2S}$ results in expression (9) as derived in Appendix A.

$$\begin{aligned}\overline{\rho_{I_1I_2S}} &= I_{1z}I_{2z} + \frac{1}{2}\left(\frac{1}{1+(y+x)^2} + \frac{1}{1+(y-x)^2}\right)ZQ_x \\ &+ \frac{1}{2}\left(\frac{y+x}{1+(y+x)^2} + \frac{y-x}{1+(y-x)^2}\right)(I_{1z} \\ &- I_{2z})S_z \\ &+ \left(\frac{1}{1+(y+x)^2} - \frac{1}{1+(y-x)^2}\right)ZQ_xS_z \\ &+ \frac{1}{4}\left(\frac{y+x}{1+(y+x)^2} - \frac{y-x}{1+(y-x)^2}\right)(I_{1z} - I_{2z}) \\ &= I_{1z}I_{2z} + \bar{a}\,ZQ_x + \bar{c}(I_{1z} - I_{2z})S_z + 2\bar{d}\,ZQ_xS_z \\ &+ \frac{1}{2}\bar{f}(I_{1z} - I_{2z}) \end{aligned} \qquad (9)$$

For convenience we introduced the dimensionless parameter $y = (J_{1S} - J_{2S})/2J_{12} = \Delta J/2J_{12}$ as a normalized measure of symmetry breaking mediated by the heteronuclear *J*-coupling. $\bar{a}$, $\bar{c}$, $\bar{d}$, $\bar{f}$ are time averaged coefficients (Appendix A). Equation (9) can be understood as a generalization of the three-spin density matrix discussed in [30] where only the heteronuclear coupling difference ΔJ has been considered as symmetry breaking mechanism.

A detectable magnetization is generated by applying an rf-pulse in *x*-direction with flip angle θ acting on spin species *I* (see Eq. 1). The resulting density matrix $\overline{\rho^{\theta}_{I_1I_2}}$ can be used to derive the NMR spectrum of the *I*-spins.

$$\begin{aligned}\overline{\rho^{\theta}_{I_1I_2}} = \sin\theta\cos\theta\ (\bar{a}-1)\left(I_{1y}I_{2z} + I_{1z}I_{2y}\right) + \sin\theta\,\bar{b}\left(I_{2y} - I_{1y}\right)S_z \\ + \sin\theta\cos\theta\ \bar{c}\left(I_{1y}I_{2z} + I_{1z}I_{2y}\right)S_z \\ + \sin\theta\ \bar{d}\left(I_{2y} - I_{1y}\right) \end{aligned} \qquad (10a)$$

If, instead, the rf-pulse is chosen to be resonant with spin species *S* then the density matrix $\overline{\rho^{\theta}_S}$ is obtained.

$$\overline{\rho^{\theta}_S} = \sin\theta\left(\bar{b}\,(I_{1z} - I_{2z})S_y + \bar{c}\,ZQ_xS_y\right) \qquad (10b)$$

We emphasize that in Eqs. (10a,b) only the components which have a nonzero contribution to the expectation value of the density matrix for spins *I* or *S* are given. The detectable FID of the nuclei can be calculated via $\langle I_{1y}+I_{2y}\rangle = Tr\left\{\overline{\rho^{\theta}_{I_1I_2}}\,(I_{1y}+I_{2y})\right\}$ or $\langle S_y\rangle = Tr\left\{\overline{\rho^{\theta}_S}\,S_y\right\}$, respectively.

In summary, we established the initial density matrices after PHIP and the action of an rf-pulse with arbitrary flip-angle θ for both two-spin and three-spin systems. This description will be used in the remainder of this article to discuss and predict observed spectral features such as amplitudes and line splittings.

3. Theory of coupled two-spin systems in the weak, strong, and inverse-weak coupling regimes

3.1 Eigenvalues

In order to predict the low-field spectra of a homonuclear *J*-coupled two-spin system we find the Eigenvalues characterizing the energy levels in the investigated spin systems and explore the transitions between these energy levels resulting in the characteristic frequencies. The general four energy-level scheme of such a spin system is shown in Fig. 2a. In high-field NMR, where B_0 is on the order of several Tesla, the chemical shift difference $\delta\upsilon$ (a few ppm for ^{1}H) exceeds the homonuclear *J*-coupling constant ($x = \delta\upsilon/J_{12} \gg 1$) and the Zeeman-effect is the dominating interaction. In this weak coupling regime, the Zeeman basis ($|\alpha\alpha\rangle, |\alpha\beta\rangle, |\beta\alpha\rangle, |\beta\beta\rangle$) adequately describes the eigenstates of the system. For low magnetic fields up to tens of milli-Tesla, chemical shift differences and *J*-coupling are often on the same order of magnitude (several Hz). Under these conditions the eigenstates are linear combinations of the Zeeman states and we enter the highly non-linear regime of strong coupling where $x \approx 1$. In particular, the states $|\alpha\beta\rangle$ and $|\beta\alpha\rangle$ mix; $|\alpha\alpha\rangle$ and $|\beta\beta\rangle$ remain eigenstates. In zero magnetic field with $B_0 = 0$, chemical shift differences are zero ($x = 0$) and the eigenstates of a two-spin system are the degenerate triplet states $|\alpha\alpha\rangle$, $\frac{1}{\sqrt{2}}[|\alpha\beta\rangle + |\beta\alpha\rangle]$, and $|\beta\beta\rangle$, and the singlet state $\frac{1}{\sqrt{2}}[|\alpha\beta\rangle - |\beta\alpha\rangle]$. We expect

exactly four dipole transitions at frequencies $\upsilon_1, \upsilon_2, \upsilon_3$ and υ_4 as shown in Fig. 2b. The frequency differences between the four spectral lines provide information about the *J*-coupling between both spins as well as their chemical shift difference. Particularly, the frequency differences $\upsilon_4 - \upsilon_1$ and $\upsilon_3 - \upsilon_2$ give access to both, the chemical shift difference and the *J*-coupling.

$$\upsilon_4 - \upsilon_1 = J_{12}\left(\sqrt{1+x^2}+1\right) \approx 2J_{12}\left(1+\frac{x^2}{4}-\frac{x^4}{16}\right) \quad (11)$$

$$\upsilon_3 - \upsilon_2 = J_{12}\left(\sqrt{1+x^2}-1\right) \approx 2J_{12}\left(\frac{x^2}{4}-\frac{x^4}{16}\right) \quad (12)$$

Note that the approximation provided in Eqs. (11) and (12) is the result of a truncated power series expansion of the square roots given in the exact solution displayed in the center.

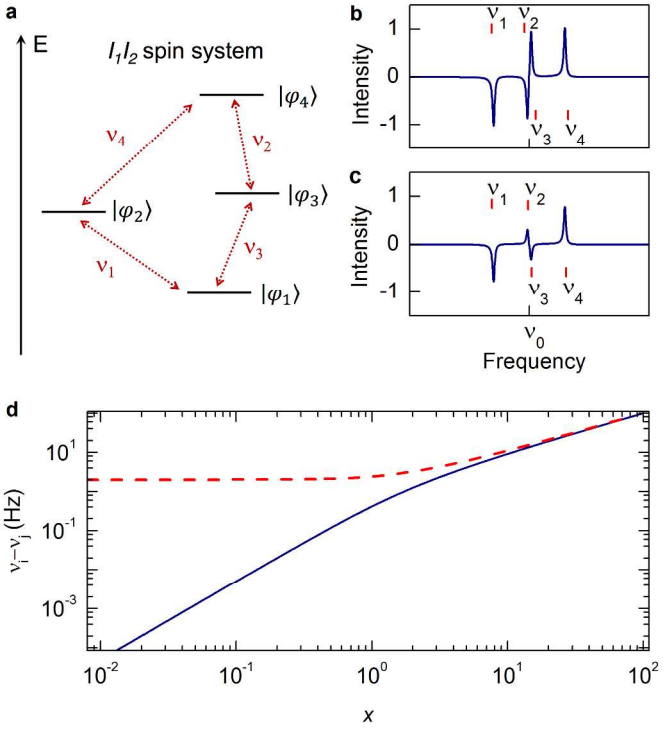

Figure 2: Energy level scheme of a coupled two-spin system I_1I_2 and its NMR spectra: (a) Energy level scheme including all allowed transitions ν_1, ν_2, ν_3, ν_4 for a parahydrogen polarized I_1I_2 system. The state vectors $|\varphi_1\rangle$,$|\varphi_2\rangle$,$|\varphi_3\rangle$ and $|\varphi_4\rangle$ correspond to the Eigenstates of the Hamiltonian $\mathcal{H}^{I_1I_2}$. State $|\varphi_2\rangle$ becomes a singlet state in zero field. (b) shows simulated NMR spectra of a two-spin system in the weak coupling and inverse weak coupling regime after $\pi/4$ pulse excitation considering a finite linewidth of 0.1 Hz. (c) Field dependencies of line splittings for $i = 4$, $j = 1$ (dashed) and $i = 3$, $j = 2$ (solid) encoding the chemical shift difference using a *J*-coupling constant of 1 Hz according to equation (11) and (12).

In a real spin system decoherence is described by a characteristic time constant T_2 and a line width of $w = 1/(\pi\, T_2)$ is observed in a spectrum. Below a critical magnetic field the inner lines at frequencies υ_2 and υ_3 begin to overlap (see Fig 2b). Under the restrictions imposed by finite linewidths these two lines cannot be resolved if $|\upsilon_3 - \upsilon_2| < w$. As a result of Eq. (11) the measurement of $\upsilon_4 - \upsilon_1$ for at least two different Larmor frequencies υ_0 yields full spectroscopic information [16, 31]. Furthermore, it is evident that the splitting is linear in x for $x \gg 1$ and highly non-linear for $x \leq 1$. In Fig. 2c the field dependence of $\upsilon_4 - \upsilon_1$ and $\upsilon_3 - \upsilon_2$ is depicted. However, the amplitude of the peaks at υ_4 and $\upsilon_1$will decrease with decreasing x in particular for thermally polarized spins, because dipole transitions between states $|\varphi_1\rangle = |\alpha\alpha\rangle$ and $|\varphi_2\rangle$ as well as between $|\varphi_2\rangle$ and $|\varphi_4\rangle = |\beta\beta\rangle$ become spin forbidden at zero magnetic field. The subsequent quantitative analysis of the observed transition probabilities and differences in initial populations highlights the stark differences between PHIP and thermally prepolarized spins.

3.2 Field and pulse dependent line amplitudes.

For a two-spin system I_1I_2 the expectation value of the detection operator $\langle \mathcal{D}_y \rangle = \langle I_{1y} + I_{2y} \rangle$ can be calculated according to Eq. (3) (neglecting decoherence/relaxation effects). The operator $I_{1y} + I_{2y}$ enables four transitions (see Fig. 2a) between the eigenstates $|\varphi_i\rangle$ of the *J*-coupled two-spin system with energy Eigenvalues E_i. Evaluating the expectation value allows assigning an amplitude A_i and a relative phase χ_i to each transition at resonance frequency υ_i as defined by

$$\langle I_{1y} + I_{2y} \rangle = \sum_{i=1}^{4} A_i \cos[2\,\pi\,\upsilon_i\, t + \chi_i]. \quad (13)$$

The explicit calculations for amplitudes and frequencies are given in appendices B and C. For a quantitative comparison of the spectral structure originating from parahydrogen and thermally polarized systems we introduce the amplitude ratio *R* as

$$R = \frac{|A_1|}{|A_2|} = \frac{|A_4|}{|A_3|} \quad (14)$$

The amplitudes of transition lines are a result of the product of transition probabilities with population differences, where only the latter are influenced by the initial state of the system determined by the polarization method. The equality of amplitude ratios in Eq. (14) follows from inspection of the four non-zero transition moments and populations differences. For PHIP the equality is perfect, for Boltzmann polarized state populations it holds only within the boundaries of the high temperature approximation. The amplitude ratio *R* may be used to quantify the roof effect, which is an important phenomenon in NMR spectroscopy for structure determination.

3.2.1 Thermal polarization. With the explicit form of the amplitudes A_i (Appendix C) the amplitude ratio R_B for a thermally (Boltzmann) polarized two-spin system can be written as a function of the coupling parameter *x*

$$R_B = \frac{\left|A_1^{\pi/2,B}\right|}{\left|A_2^{\pi/2,B}\right|} = 1 - \frac{2}{x^2}\left(\sqrt{1+x^2}-1\right), \quad (15)$$

where $A_i^{\pi/2,B}$ is the amplitude of a transition line at frequency υ_i after $\pi/2$ excitation. As a result of Eq. (15) the two outer transition lines with amplitudes A_1 and A_4 vanish for $x \to 0$ due to the decreasing transition probabilities between states $|\varphi_1\rangle$, $|\varphi_2\rangle$ as well as $|\varphi_2\rangle$, $|\varphi_4\rangle$. At high fields, $x >> 1$, the amplitude ratio R_B converges to 1. Equation (15) can thus be understood as analytical expression describing the roof effect for a two-spin system [25]. It can be seen from Eq. (15) that $R_B \to 0$ for $x \to 0$ rendering J_{12} and $\delta\upsilon$ unobservable.

3.2.2 Parahydrogen induced polarization. We limit the discussion of the amplitude ratios to $R_{PHIP}^{\pi/4} = \left|A_1^{\frac{\pi}{4},PHIP}\right| / \left|A_2^{\frac{\pi}{4},PHIP}\right|$ after $\pi/4$ and $R_{PHIP}^{\pi/2} = \left|A_1^{\frac{\pi}{2},PHIP}\right| / \left|A_2^{\frac{\pi}{2},PHIP}\right|$ after $\pi/2$ pulse excitation, as they constitute the most frequently used excitation pulses for PHIP and Boltzmann polarized spin systems. As shown in Appendix C, a two-spin system prepared with a $\pi/2$ pulse has identical absolute amplitudes of all four transition lines ($R_{PHIP}^{\pi/2} = 1$).

$$A_1^{\frac{\pi}{2},PHIP} = A_2^{\frac{\pi}{2},PHIP} = -A_3^{\frac{\pi}{2},PHIP} = -A_4^{\frac{\pi}{2},PHIP} \quad (16)$$

Assuming an infinitely small line width ($T_2 \to \infty$) the amplitude ratio $R_{PHIP}^{\pi/2}$ is independent of x. Therefore, the population differences of the states compensate the different transition probabilities for the transitions υ_1, υ_2 and υ_3, υ_4 (see Fig. 2a). Due to the anti-Zeeman term $(I_{2y} - I_{1y})$ of the two-spin density matrix in Eq. (7) remaining after $\pi/2$ x-pulse excitation the amplitude pairs A_1, A_2 and A_3, A_4 are of opposing sign.
When implementing a $\pi/4$ excitation pulse the amplitude ratio $R_{PHIP}^{\pi/4}$ remains a function of the coupling parameter x.

$$R_{PHIP}^{\pi/4} = \left|1 - \frac{2}{1 + (\sqrt{2}-1)\sqrt{1+x^2}}\right| \quad (17)$$

Note that expression (17) is zero and has a discontinuity at $x_D = \sqrt{2(1+\sqrt{2})}$. This is caused by a change of sign of the inner two transition lines υ_2 and υ_3 at x_D which corresponds to zero amplitude of A_2 and A_3. Irrespective of the applied excitation pulse angle the amplitudes of the inner lines are phase shifted by π. In the vicinity of x_D the amplitudes A_2 and A_3 are very small compared to A_1 and A_4 – as opposed to the roof effect discussed for Boltzmann polarized spins. Overlap of the inner transition lines occurring in the inverse weak coupling regime due to finite T_2 lifetimes effectively results in destructive interference of the signals for any excitation pulse (see Fig. 2b). Quantitatively, this cancelation can be described by evaluating the integral $\mathcal{S}_{\upsilon 23}$ of the superposition of the two central Lorentz shaped peaks $\mathcal{L}_3$ and $\mathcal{L}_2$ of opposite sign with their respective center frequencies separated by $\upsilon_{23} = \upsilon_2 - \upsilon_3$. The superposition integral $\mathcal{S}_{\upsilon 23}$ can be expressed as a function of x.

$$\mathcal{S}_{\upsilon 23} = \int_0^\infty \left(\mathcal{L}_3\left[\upsilon; \frac{\upsilon_{23}}{2}\right] - \mathcal{L}_2\left[\upsilon; -\frac{\upsilon_{23}}{2}\right]\right) d\upsilon = \frac{2}{\pi} arctan\left[\pi\ T_2\ J_{12}\left(\sqrt{1+x^2}-1\right)\right] \quad (18)$$

We refer to this inverted behavior of the line amplitudes as inverse roof effect, which can be written as

$$R_{PHIP}^{\pi/2} = {\mathcal{S}_{\upsilon_{23}}}^{-1} \quad (19a)$$

for $\pi/2$ x-pulse excitation and

$$R_{PHIP}^{\pi/4} = \left|1 - \frac{2}{1 + (\sqrt{2}-1)\sqrt{1+x^2}}\right| {\mathcal{S}_{\upsilon_{23}}}^{-1}. \quad (19b)$$

for $\pi/4$ pulse excitation. In Fig. 3a the amplitude ratios for thermally and parahydrogen polarized spin systems are plotted as a function of x.
In the following we examine the signal-to-noise ratio (*SNR*) for both parahydrogen and thermally polarized spins in order to determine a lower limit of the required magnetic field strength to render the inverse roof effect observable.

3.3 SNR-Model for PHIP and thermal polarization

For low-field NMR experiments it is appropiate to assume that the dominating noise source is Johnson noise $\sim\sqrt{4\,k_B T\,R_S\,\Delta\nu_D}$ from the detection coil with AC-resistivity R_S. The minimal detection bandwidth $\Delta\nu_D$ needs to cover at least the total spectral width of the *J*-coupled two-spin spectrum. For pre-magnetized and hyperpolarized spins with distinct polarization P and using $\Delta\nu_D = J_{12}\left(1+\sqrt{1+x^2}\right)$ (see Eq. (11), Appendix B and C) the *SNR* model in [32] can be modified to account for the different origins of the polarisation P to yield

$$SNR = \frac{k_0\gamma_I(B_1/i)N_S\hbar\gamma_I B_0 P}{2\sqrt{2}\sqrt{4\,k_B T\,R_S\,\Delta\nu_D}} = \alpha\frac{x}{\sqrt{1+\sqrt{1+x^2}}}\sum_i |A_i|. \quad (20)$$

A_i are the amplitudes of the transitions as derived in Appendix C [32, 33] and the coefficient α

$$\alpha = \frac{\hbar k_0\gamma_I(B_1/i)N_s\sqrt{2\pi J_{12}}P}{\sqrt{2}\sqrt{4k_B T R_s}(\delta_2 - \delta_1)} \quad (21)$$

contains all field independent factors, such as the coil sensitivity B_1/i, the filling factor k_0, the number of spins N_s in the sample and the chemical shift difference $(\delta_2 - \delta_1)$. Note that the polarization P is B_0-field independent as it may originate from any hyperpolarization method. In practice there are several additional noise sources which are mainly caused by peripheral electronics. This is covered by a constant factor α' which is determined experimentally for each polarization method.
As a result of the right hand side of Eq. (20) the *SNR* is linear in x for $x << 1$ and proportional to $\sqrt{x}$ for $x >> 1$. This is illustrated in Fig. 3 b where $\alpha \approx 4$ covers typical experimental parameters for ^{1}H-NMR experiments with spins prepolarized at 2 T and T = 300 K ($P = 6 \times 10^{-6}$).

3.3.1 Thermal polarization without pre-magnetization. Experiments which do not entail pre-magnetization have a more pronounced field dependence of the *SNR* than a PHIP experiment because the polarization P is a function of the external magnetic field strength. In the high temperature approximation ($k_B T \gg \hbar\gamma_I B_0$) P is linear in x for a given molecule. Using $\Delta\nu_D$ as the minimal bandwidth and $\sum_i |A_i| = 1$ for Boltzmann polarized spins (see Appendix C) we get

$$SNR_B = \alpha_B\frac{x^2}{\sqrt{1+\sqrt{1+x^2}}}, \quad (22)$$

where the prefactor for Boltzmann-polarization, as well as all parameters covered by Eq. (21), are included in α_B.

3.3.2 Parahydrogen induced polarization. After chemical reduction of a molecule with parahydrogen the singlet symmetry is broken by a chemical shift difference and an initial density matrix $\overline{\rho_p}$ is formed according to Eq. (7). This generates a measureable polarization

expressed as $I_{1z}I_{2z}$ and $I_{1z} - I_{2z}$. In the experiment, the process takes place with constant parahydrogen pressure as well as fixed amounts of catalyst and substrate. These conditions allow to introduce a parameter α_{PHIP} which combines reaction rates in the initial stages of the chemical reaction and all noise sources. Using Eq. (7) for the initial density matrix and the minimal bandwidth $\Delta\nu_D$ defined above we obtain the *SNR* after a $\pi/2$ pulse to

$$SNR_{PHIP}^{\pi/2} = \alpha_{PHIP}^{\pi/2}\left(\frac{x}{\sqrt{1+\sqrt{1+x^2}}}\right)\left(\frac{x^2}{(1+x^2)^{3/2}}\right). \quad (23)$$

The first bracket on the right hand side of Eq. (23) is in analogy to Eq. (20) and includes Faraday-detection and Johnson noise with limited bandwidth $\Delta\nu_D$. The second bracket is the explicit form of the sum over transition line amplitudes in Eq. (20) using Eq. (7) (see Appendix C and D).

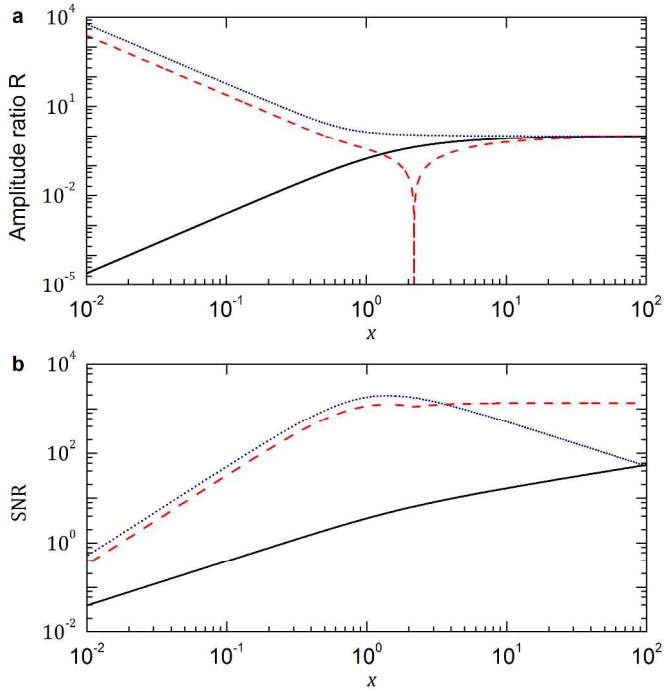

Figure 3: Effective amplitude ratio *R* (a) and *SNR* (b) of a two-spin system I_1I_2 as a function of x for thermally polarized spins (solid), parahydrogen polarized spins after $\pi/2$ (dotted) and $\pi/4$ (dashed) excitation using T_2 = 3 s, J_{12} = 8.5 Hz and $\delta_2 - \delta_1$ = 2.46 ppm.

For a $\pi/4$ pulse excitation the sign change of the amplitudes A_i at $x_D = \sqrt{2(1+\sqrt{2})}$ requires the distinction between two regimes of x.

$$SNR_{PHIP}^{\frac{\pi}{4}} = \alpha_{PHIP}^{\frac{\pi}{4}}\left(\frac{x}{\sqrt{1+\sqrt{1+x^2}}}\right)\left(\frac{x^2}{4(1+x^2)}\right),$$

$$\text{if } x > \sqrt{2(1+\sqrt{2})} \quad (24a)$$

$$= \alpha_{PHIP}^{\frac{\pi}{4}}\left(\frac{x}{\sqrt{1+\sqrt{1+x^2}}}\right)\left(\frac{(1+\sqrt{2})x^2}{4(1+x^2)^{\frac{3}{2}}}\right),$$

$$\text{if } x < \sqrt{2(1+\sqrt{2})} \quad (24b)$$

Figure 3b shows the *SNR* as a function of x using Eqs. (23-24) for PHIP and both pulse excitations (dotted and dashed line). A $\pi/2$ pulse yields a 1.6 times higher SNR compared to the $\pi/4$ pulse for $x < 1$, whereas for $x >> 1$ the *SNR* is highest for $\pi/4$ excitation pulses. The pronounced maximum of the *SNR* for $\pi/2$ excitation at $x = 2\sqrt{2}$ is a result of the third term on the right hand side of the density matrix in Eq. (7) [16]. It is immediately evident from Fig. 3b that for $10^{-2} < x < 10^2$ the SNR obtained in an NMR experiment using parahydrogen polarization is far superior to thermal prepolarization when assuming feasible magnetic field strengths.

4. Polarization transfer pathways in *J*-coupled I_1I_2S spin systems

Polarization transfer from high γ nuclei (e.g. ^{1}H, ^{19}F) to low γ spins of low natural abundance (e.g. ^{13}C, ^{29}Si) is of great relevance due to the significant increase of structural information gained from coupled and decoupled rare spin spectra. Established methods making use of high thermal polarization are Hartmann-Hahn Cross-Polarization (CP) or Insensitive Nuclei Enhancement by Polarization Transfer (INEPT) [34, 35]. In more recent developments the singlet spin-order of parahydrogen available in PHIP or SABRE experiments has been proven to be an ideal source for polarization which can be transferred to rare spins [36-40].

As a result of Eq. (8) polarization transfer to rare spins is an intrinsic property of the spin system when appropriate matching conditions are met. A non-zero value of the expectation value of the *S* magnetization after a $\pi/2$ *x*-pulse results from the third and fourth term on the right hand side of Eq. (9), giving

$$\langle S_y\rangle = Tr\left[S_y\{\bar{b}\,(I_{1z}-I_{2z})S_y + \bar{c}\,ZQ_xS_y\}\right]. \quad (25)$$

In order to facilitate discussion of the polarization transfer pathways we recall that the coefficients $\bar{b}$ and $\bar{c}$ are functions of the parameters $x = \delta\upsilon/J_{12}$ and $y = (J_{1S} - J_{2S})/2J_{12} = \Delta J/2J_{12}$.

$$\bar{b}(x,y) = \frac{1}{2}\left(\frac{y+x}{1+(y+x)^2} + \frac{y-x}{1+(y-x)^2}\right) \quad (26a)$$

$$\bar{c}(x,y) = \left(\frac{1}{1+(y+x)^2} - \frac{1}{1+(y-x)^2}\right) \quad (27a)$$

The coefficients $\bar{b}$ and $\bar{c}$ depend on the magnitude of the magnetic field and hetero- and homonuclear *J*-coupling constants and reflect the amplitudes of spectral lines of the *S*-spin spectrum after polarization transfer from parahydrogen. While the parameter y depends only on the molecular structure, x varies with the magnetic field B_0. Analyzing the dependence of $\bar{b}$ and $\bar{c}$ on x, using y as a fixed parameter as it is constant for a specific molecule, allows to determine in which magnetic field strength polarization transfer to heteronuclei occurs with highest efficiency, thereby defining matching conditions. Figures 4 (a, b) show a contour plot of the magnitude of coefficients $\bar{b}$ and $\bar{c}$ associated with the polarization of the *S*-spin, where the coefficient $\bar{b}$ may take values from {-0.5, 0.5} and $\bar{c}$ from {-1, 1}. The plots in Fig. 4 a and b use logarithmic axis scaling in x and y to allow for identification of extreme values over a large range of parameter combinations. The contour plot of coefficient $\bar{c}$ as a function of x and y in Fig. 4 b shows that for $x << 1$ no value of y exists for efficient polarization transfer from parahydrogen to the *S*-spin. For $x \geq 1$ there is a relative minimum along $x = y$ with $\bar{c} = -1$, defining the first matching condition $\gamma_I B_0(\delta_2 - \delta_1) = (J_{1S} - J_{2S})/2$. Hence, there is exactly one field B_0 for a given chemical compound, identified by exactly one value of y,

resulting in maximum polarization transfer, which occurs even in case the chemical shift difference between spin I_1 and I_2 is not negligible.

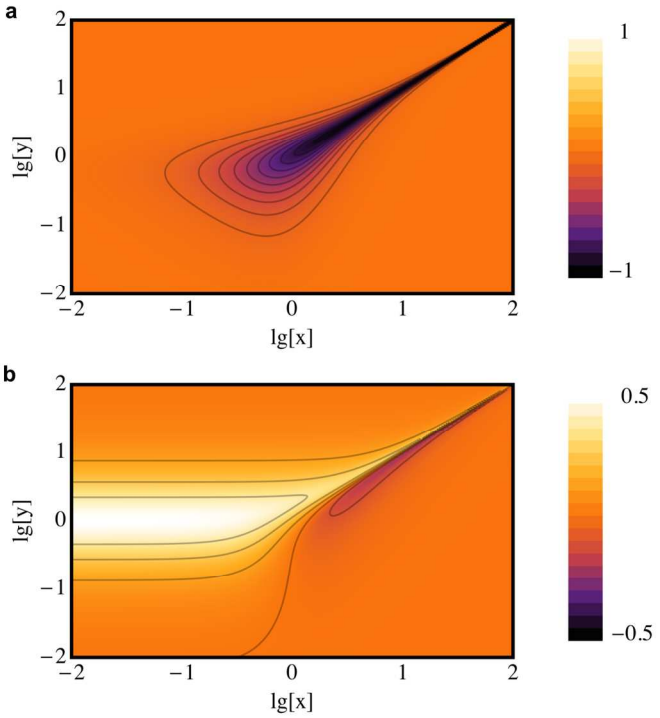

Fig. 4: (a) Contour plot of coefficient $\bar{b}$, associated with term $(I_{1z} - I_{2z})S_z$. (b) Contour plot for coefficient $\bar{c}$, associated with ZQ_xS_z. (a) allows to identify matching conditions for polarization transfer in low magnetic fields $x << 1$ found at $y = 1$, (b) allows to identify matching condition $x = y$ for high magnetic fields (see text for explanation). Note the logarithmic scale covering a large range of x and y.

The dependence of coefficient $\bar{b}$ on x and y is more complex (see Fig. 4a). For $x >> 1$ the value of $\bar{b}$ changes its sign when passing the contour line $x = y$ where $\bar{b} = 0$. This means that very slight deviations from $x = y$ will result in observable polarization transfer. At low magnetic fields, $x << 1$, a maximum value of $\bar{b} = 0.5$ exists at $y = 1$. This means, that polarization transfer from parahydrogen to S is maximal and nearly constant down to zero field if the second matching condition $(J_{1S} - J_{2S})/2 = J_{12}$, or $y = 1$, is fulfilled. The second matching condition is of special relevance for polarization transfer experiments in low magnetic fields described in section V.

5. Experimental studies: Coupled two-spin I_1I_2, three-spin I_1I_2S and four-spin systems $I_1I_2I_3$S

The experiments were performed using a home built NMR spectrometer which operates at variable magnetic flux densities ranging from 3.9 to 18.8 mT, while maintaining sub-ppm field homogeneity over the sample dimensions of 0.36 cm^3 on a timescale of several minutes. The detections coils are modular and can be exchanged to obtain maximum *SNR* at the resonance frequency of the investigated nucleus at a chosen field strength. Parahydrogen (92.8 %, 32 K conversion temperature) is generated using a commercially available BPHG090 system (Fa. Bruker Biospin). Samples are prepared using 0.4 mg of the rhodium catalyst ([1,4-Bis(diphenylphosphino)butane](1,5-cyclooctadiene)-rhodium(I)tetrafluoroborate) and 20 µL of the spin system of interest dissolved in 340 µL anhydrous acetone-d_6. In PHIP experiments the sample was subjected to 5 atmospheres of parahydrogen and the solution was shaken (5 - 10 seconds) at the 5 G stray field for ^{1}H experiments and in a double layered μ-metall chamber ($B \leq 0.002$ G) for ^{13}C experiments. The samples were transferred to the homogeneous field in the center of the shimmed electromagnet within a transfer time of 2 s (Fig. 5 a). After excitation with a pulse of flip angle θ the free induction decay (FID) was detected with a coil tuned to the resonance frequency. After preamplification the FID was amplified with a lock-in amplifier operating close to the Larmor-frequency and the signal was recorded via a data acquisition card.

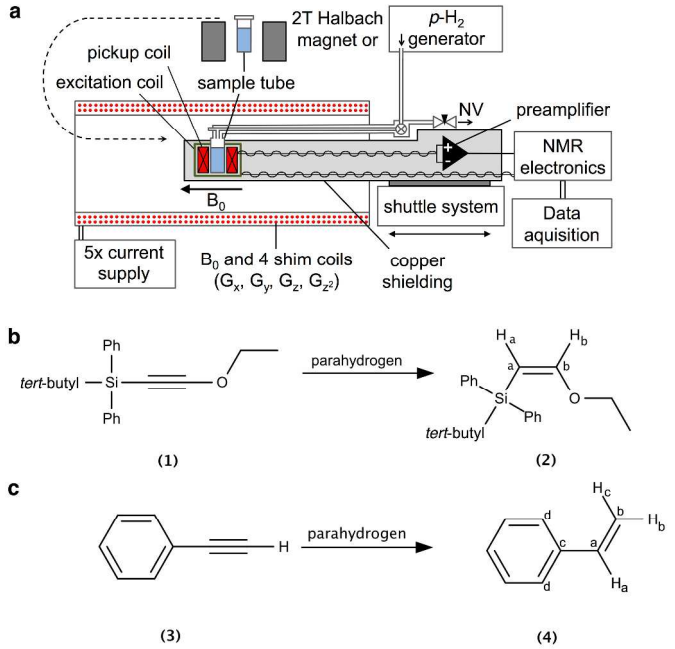

Fig.5: (a) Experimental setup including homebuilt NMR spectrometer, parahydrogen supply and detection electronics. b) Hydrogenation of ethoxyethyne dervitate (**1**) to ethylene derivate (**2**) leads to a homonuclear *J*-coupled two-spin system I_1I_2 (H_aH_b) and naturally abundant heteronuclear *J*-coupled three-spin systems I_1I_2S ($^{13}C_aH_aH_b$, $^{13}C_bH_aH_b$, $^{29}SiH_aH_b$). (c) Hydrogenation of phenylacetylene (**3**) to styrene (**4**) leading to three-spin system $I_1I_2I_3$ and four-spin systems $I_1I_2I_3S$ ($^{13}C_aH_aH_bH_c$, $^{13}C_bH_aH_bH_c$).

Experimental studies were performed with a disubstituted ethyne molecule 1-(*tert*-butyldiphenylsilyl)-2-(ethoxy)ethyne (**1**) and commercially available phenylacetylene (**3**). The ethyne derivate (**1**) was designed to form a model, upon hydrogenation (**2**) (see Fig. 5b), for a homonuclear *J*-coupled two-spin system I_1I_2 with a large chemical shift difference (H_aH_b: 93.3%). Additionally, hydrogenation to (**2**) forms three important heteronuclear *J*-coupled three-spin systems I_1I_2S ($S = ^{29}$Si, ^{13}C; $I_j = ^1$H), present at the natural abundance of ^{13}C and ^{29}Si respectively ($H_aH_b{}^{29}$Si: 4.7%, $H_aH_b{}^{13}C_a$: 1%, $H_aH_b{}^{13}C_b$: 1%) [16].

Phenylacetylene (**3**) is a model for a homonuclear three spin system $I_1I_2I_3$ and two distinct four spin systems $I_1I_2I_3S$ ($S = ^{13}$C; $I_j = ^1$H), formed after hydrogenation to styrene (**4**) (see Fig. 5 c). The first compound provides experimental proof for the spectra derived from the theoretical description of the three-spin density matrix in Eq. (9), the second compound provides proof for the matching conditions defined in equations (26a,b) [16,41].

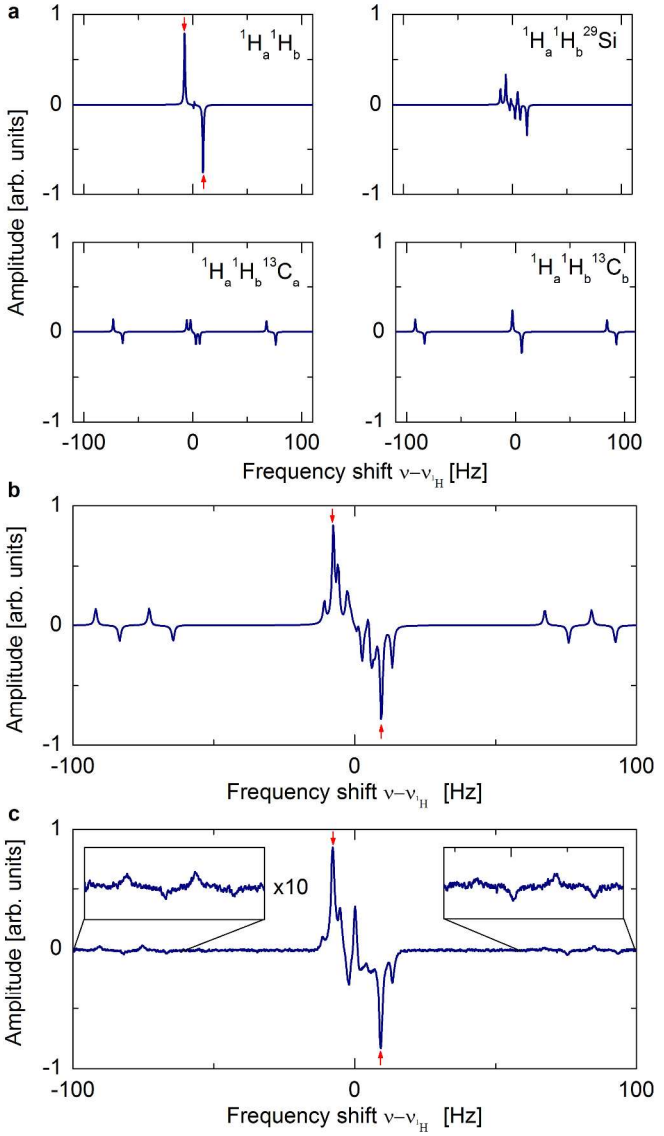

Fig.6: (a) Simulated ^{1}H spectra of the pseudo two-spin system consisting of the four isotopomers $^1H_a{}^1H_b$, $^1H_a{}^1H_b{}^{29}Si$, $^1H_aH_b{}^{13}C_a$ as well as $^1H_a{}^1H_b{}^{13}C_b$. The complete ^{1}H spectrum is shown in (b) where the isotopmers are weighted by their natural abundances. Panel (c) shows the experimentally measured spectrum with ten times magnified insets of the ^{13}C satellites at 500 kHz proton resonance frequency. The arrows indicate the transition lines ν_1 and ν_4 of the homonuclear two-spin system.

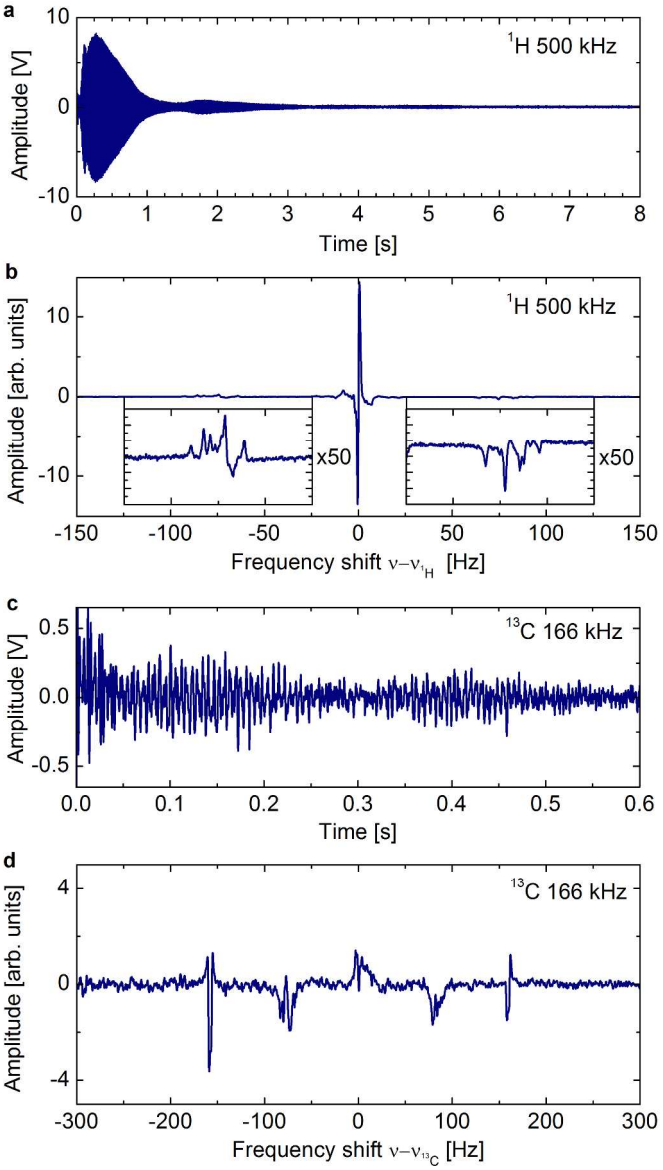

Fig. 7: Experimental data of hyperpolarized styrene: (a) FID of the proton signal at 500 kHz Larmor frequency after $\pi/2$ excitation pulse. (b) Corresponding ^{1}H spectra with fine structure due to heteronuclear *J* coupling. (c) FID of ^{13}C at 166 kHz Larmor frequency after $\pi/2$ excitation detected in single shot. Mind that the signal strength is associated with Eq. (10b). (d) ^{13}C spectrum revealing local spectroscopic information.

First, we discuss the PHIP spectra obtained with the disubstituted ethyne molecule (**2**). The *J*-coupling constants are $^3J_{HaHb} = 8.5$ Hz, $^1J_{HaCa} = 140.7$ Hz, $^1J_{HbCb} = 177.9$ Hz, $^3J_{HbSi} = 11.0$ Hz, $^2J_{HaSi} = -0.5$ Hz and the chemical shift difference between H_a and H_b is $\delta_2 - \delta_1 = 2.46$ ppm. The two-spin system was designed such that at 500 kHz ^{1}H frequency $x = \delta\nu/J_{12} = 0.15$, which is sufficiently high to yield enough *SNR* to be observable in a single scan (Fig. 4b). Figure 6a shows simulated ^{1}H-spectra based on the three spin density matrix (Eq. 9) of all four isotopomers using $\pi/4$ excitation pulses. The superposition of the isotopomer subspectra weighted by their respective natural abundances (Fig. 6b) is in agreement with the experimentally observed ^{1}H spectrum (Fig. 6c). The arrows in Fig. 6a,b,c indicate the positions of spectral lines at υ_1 and υ_4, where we expect non-linear field dependence on *x* for the frequency difference $\upsilon_4 - \upsilon_1$ in accordance with Eq. (11) [16].

Next, we consider PHIP spectra of styrene (**4**). The ^{1}H PHIP spectra can be assigned to a three-spin system $H_aH_bH_c$ and two four spin systems $H_aH_bH_c{}^{13}C_a$ and $H_aH_bH_c{}^{13}C_b$ if we assume that the observed polarization stems only from the nuclei close to the double bond. Figures **7**a and b show the FID and the ^{1}H-spectrum of parahydrogen enhanced styrene NMR signal at 500 kHz resonance frequency after $\pi/2$ pulse excitation, where the *SNR* obtained in a single shot is 285. The spectrum is dominated by a narrow, high amplitude anti-phase peak at the center frequency ν_{1H}. In addition we observe two groups of peaks (zoomed-in insert) covering a spectral width of 34 Hz each and shifted by ±77 Hz from the center frequency ν_{1H}. They exhibit an anti-symmetric structure with respect to the center frequency. These two groups of peaks are caused by the superposition of the $H_aH_bH_c{}^{13}C_a$ and $H_aH_bH_c{}^{13}C_b$ subspectra.
The nucleus $^{13}C_a$ in the corresponding isotopomer gives rises to a doublet separated by the heteronuclear coupling constant

$^1J_{HaCa}$ = 154.0 Hz. Homonuclear *J*-couplings ($^3J_{HaHc}$ = 17.6 Hz, $^3J_{HaHb}$ = 11.0 Hz) split each line of the heteronuclear doublet into a doublet of doublets. The anti-symmetric line structure results mainly from the term associated with coefficient $\bar{b}$ in the three-spin density matrix (Eq. 9) where the signal after a θ pulse is given by Eq. (10b). The dominant structure of the C_b isotopomer spectrum consists of two doublets spaced by $^1J_{HbCb}$= 160.0 Hz and $^1J_{HcCb}$ = 154.6 Hz. In this case, the lines associated with H_c contribute a doublet of doublets with $^3J_{HaHc}$ = 17.6 Hz and $^2J_{HbHc}$ = 1.0 Hz; likewise the lines for H_b are split into a doublet of doublets by $^3J_{HaHb}$ = 11.0 Hz and $^2J_{HbHc}$= 1.0 Hz. The splitting of 1 Hz is poorly resolved due to finite linewidths of ~1 Hz. All line positions are in reasonable agreement with simulations based on the superposition of three-spin density matrices as an approximation to the density matrices of hetero- and homonuclear *J*-coupled four spin systems $H_aH_bH_c{}^{13}C_b$ and $H_aH_bH_c{}^{13}C_a$. Additionally, the exact values agree with high field measurements performed at 400 MHz ^{1}H resonance frequency and the long range coupling constants published in [42]. The structure of the groups of peaks in a range from -20 to 20 Hz around the centre frequency ν_{1H} can be explained in a similar fashion but determination of the exact line position is more difficult, as hetero- and homonuclear coupling constants have similar magnitude resulting in asymmetric line splitting in the strong coupling limit.
The occurrence of a large central line at ν_{1H} in Fig 7b is most likely a result of 92% of molecules without hetero spins. In the evolution period at 5 G the homonuclear *J*-coupling network distributes the H_aH_b singlet over the entire molecule and $x < 0.1$ for all possible proton singlet pairs. Upon transfer to the measurement field of 120 G (ν_{1H} = 500 kHz) $x \approx 0.5$ for long range singlets such as H_aH_d ($^4J_{HaHd} \approx 0.5$ Hz and $\delta\upsilon \approx 0.25$ Hz) using $\delta_{Ha} = 6.89$, $\delta_{Hd} = 7.45$ ppm of styrene [43]. This value of x gives rise to a large *SNR* and superposition of spectra associated with all long range singlets would result in a large peak with anti-phase structure close to the center frequency, thus accounting for both the large amplitude and the phase of the dominating peak in Fig. 7b. This point will attract further investigation in the future, as long range singlet states are of interest for magnetic resonance imaging and quantum information processing.

In the following we provide a qualitative explanation of the PHIP spectrum of ^{13}C in styrene based on the analytical form of the three-spin density matrix introduced above. The polarisation pathways derived in section IV agree with our experimental results, though the experimental system consists out of four spins. Figure 7 c,d show the FID and the ^{13}C spectrum of styrene at 166 kHz Larmor frequency using a $\pi/2$ pulse excitation. Note that a *SNR* of 15 is obtained in a single scan, although the reactant phenylacetylene contains ^{13}C in natural abundance (1%) and the sensitivity of the NMR setup is lower at 166 kHz. This indicates an efficient polarization transfer from parahydrogen to the rare spin ^{13}C. Remembering that $y = (J_{1S} - J_{2S})/2J_{12} = \Delta J/2J_{12}$ depends only on the *J*-coupling parameters, we introduce y_{abc} for each isotopomer identifying the specific nuclei, where indices correspond to the positions defined in Fig. 5c.
If we approximate the system of four coupled spins by a superposition of three-spin systems there are six possible values for the parameter *y* as defined in Eq. (24): Using the ^{1}H chemical shifts of $\delta_{Ha} = 6.89$, $\delta_{Hb} = 5.39$, $\delta_{Hc} = 5.93$ allows to calculate y_{CbHaHb} = 7.3, y_{CbHaHc} = 4.4, y_{CbHbHc} = 2.7 y_{CaHaHb} = 7.0, y_{CaHaHc} = 4.5 and y_{CaHbHc} = 2.25. The matching condition responsible for polarisation transfer at low field is dominated by coefficient $\bar{b}$, which approaches values close to the theoretical maximum of 0.5. Considering the magnetic field strength of the evolution field, in which the hydrogenation takes place in case of ^{13}C experiments, is B_0 smaller than 0.002 G, we obtain $\bar{b}_{CaHbHc} = 0.44$ and $\bar{b}_{CbHbHc} = 0.37$ as upper limits and $\bar{b}_{CbHaHb} = 0.13$ as lower limit. The crossing condition with $y = 1$ is best met for the geminal hydrogen atoms H_b and H_c with respect to both ^{13}C positions. The similarity in areas under the peak structures in Fig. 7 d can be explained by the similar values calculated for $\bar{b}$, where $\bar{b}_{CaHaHb} \approx \bar{b}_{CbHaHb}$ and $\bar{b}_{CaHbHc} \approx \bar{b}_{CbHbHc}$. Results of prior investigations on the hydrogenation of phenylacetylene with the catalyst used in our experiments suggest that rapid hydrogen exchange occurs in the side chain of styrene [41]. As a result of hydrogen exchange and exposure to zero field [20] the existence of singlets other than H_aH_b, such as H_aH_c or H_bH_c, is also possible as already indicated by the large central peak observed in ^{1}H spectra.

The main features of the ^{13}C spectrum can be described by a triplet corresponding to the C_b isotopomer and a doublet identifying the C_a isotopomer. The groups of lines for both the C_a and the C_b isotopomers are separated by heteronuclear *J*-coupling constants of 150-160 Hz. Close inspection of the spectrum reveals that the center frequencies of the doublet and the triplet are shifted by approximately 4 Hz with respect to each other. This is a result of the chemical shift difference $\delta_{Ca} - \delta_{Cb} = 23.6$ ppm between the ^{13}C positions a and b. The spectral lines of the $^{13}C_a$ isotopomer subspectrum (doublet, $^1J_{HaCa}$ = 154.0 Hz) are additionally split by $^2J_{HcCa}$ = -4.5 Hz ($^2J_{HbCa}$ is negligible and causes no further fine structure).
For the $^{13}C_b$ isotopomer heteronuclear coupling is anisochronous ($^1J_{HbCb} \neq {}^1J_{HcCb}$) but the ^{1}H nuclei are nearly isogamous ($\nu(H_b) = \nu(H_c)$ - 0.3 Hz) at a ^{13}C resonance frequency of 166 kHz. If *J*-coupling constants have similar magnitude ($^1J_{HbCb}$ = 160.0 Hz, $^1J_{HcCb}$= 154.6 Hz) the coupling pattern is approximately a triplet, as observed in the spectrum. The structure close to the center frequency $\nu = \nu_{13C}$ is split in two groups of lines separated by about $^1J_{HbCb}$ - $^1J_{HcCb}$ = 5.4 Hz. The outer lines are split by $\pm$158 Hz. Note that this line splitting corresponds to neither $^1J_{HcCb}$ or $^1J_{HbCb}$ [27].
In this section we demonstrated that the combined ^{1}H and ^{13}C spectra allow for identification of the ethylene group and we have shown that it is possible to determine *J*-coupling constants as well as chemical shifts in good agreement with high field data. Therefore, our low field apparatus enables identification of the local chemical structure.

6. Conclusions

In conclusion we have derived the analytic description of symmetry breaking mechanisms for PHIP at low and high fields for homonuclear two-spin systems I_1I_2 and heteronuclear three-spin systems I_1I_2S. The density matrix formalism allows us to extract amplitudes and phases of transition lines. Furthermore, two fundamental polarization transfer pathways were identified enabling NMR spectroscopy on naturally abundant rare spins without using pulse sequences or field cycling methods [29, 30, 38-41, 44, 45]. Based on the analytical description of the two-spin density matrix an *SNR* model as a function of the magnetic field has been developed for arbitrary excitation pulse angles. This *SNR* model combined with a detailed analysis of spin state populations give rise to the inverse roof effect, which enables determination of chemical shift and *J*-coupling constants down to very low magnetic fields. Experimental data of parahydrogen polarized two-spin, three-spin and four-spin systems show good agreement with theory. The theoretical foundations and experimental evidences presented in this article are a further milestone for low field NMR spectroscopy, which might lead to low-cost, portable spectrometers for chemical analysis.

Understanding initialisation and symmetry breaking mechanisms with many singlets entangled on length scales ranging from Ångströms to a few nanometers is of general interest for future developments in quantum information processing. The knowledge of density matrices of more complex spin systems serves as foundation for synthesizing molecules optimized for polarization storage in form of rare spin singlets ($^{13}C^{13}C$, $^{15}N^{15}N$). This will enable background free imaging even in very low magnetic fields [37], which is beneficial as some relaxation pathways are less pronounced [42, 44, 46].

Acknowledgements

We thank Stefan Glöggler for his assistance, Phillip Schleker, Jürgen Klankermayer from the ITMC as well as Dmitry Budker and Micah Ledbetter from University of California, Berkeley for their help. The authors gratefully acknowledge technical assistance from J. Schmitz, S. van Waasen, G. d'Orsaneo, A. Schwaitzer from the Forschungszentrum Jülich and we thank J. M. Tyburn, J. Lohmann, and D. Kilgour from Bruker Biospin GmbH for support of the Bruker BPHG090 Parahydrogen Generator. T.T. thanks the ERS for funding in form of the Theodore-van-Karman Fellowship. Parts of this work were funded by the Excellence Initiative of the German federal and state government.

.

Notes and references

[a] Institut für Technische und Markomolekulare Chemie, RWTH Aachen University, 52056 Aachen, Germany.

[b] Max Planck Institute for the Science of Light, 91058 Erlangen, Germany.

[c] Department of Chemistry, Duke University, Durham, NC 27708 USA.

[d] Zentralinstitut für Engineering, Elektronik und Analytik, Systeme der Elektronik (ZEA-2), Forschungszentrum Jülich, 52425 Jülich, Germany.

Electronic Supplementary Information (ESI) available: Details on the calculation are provided in appendices a-d. See DOI: 10.1039/b000000x/

1 T.G. Walker, and W. Happer, *Rev. Mod. Phys.* 1997, **69**, 629.

2. S. Appelt, A. Ben-Amar Baranga, C. J. Erickson, M. V. Romalis, A. R. Young and W. Happer, *Phys. Rev. A* 1998, **58**, 1412.
3. T. R. Carver and C. P. Slichter, *Phys. Rev.* 1956, **102**, 975.
4. C. R. Bowers and D. P. Weitekamp, *Phys. Rev. Lett.* 1986, **57**, 2645.
5. R.W. Adams, J. A. Aguilar, K. D. Atkinson, M. J. Cowley, P. I. P. Elliott, S. B. Duckett, G. G. R. Green, I. G. Khazal, J. Lopez-Serrano and D.C. Williamson, *Science* 2009, **323**, 1708.
6. R. McDermott, A. H. Trabesinger, M. Mueck, E. L. Hahn, A. Pines and J. Clarke, *Science* 2002, **295**, 2247.
7. I. K. Kominis, T. W. Kornack, J. C. Allred and M. V. Romalis, *Nature* 2003, **422**, 596.
8. D. Sheng, S. Li, N. Dural and M. V. Romalis, *Phys. Rev. Lett.* 2013, **110**, 160802.
9. F. Jelezko, T. Gaebel, I. Popa, M. Domhan, A. Gruber and J. Wrachtrup, *Phys. Rev. Lett.* 2004, **93**, 130501.
10. J. M. Taylor , P. Cappellaro , L. Childress , L. Jiang , D. Budker , P. R. Hemmer , A. Yacoby , R. Walsworth and M. D. Lukin, *Nat. Phys.* 2008, **4**, 810.
11. T. Staudacher, F. Shi, S. Pezzagna, J. Meijer, J. Du, C. A. Meriles, F. Reinhard and J. Wrachtrup, *Science* 2013, **339**, 561.
12. C. L. Degen, M. Poggio, H. J. Mamin, C. T. Rettner and D. Rugar**,** *Proc. Natl. Acad. Sci. USA* 2009, **106**, 1313.
13. S. Appelt, H. Kühn, F. W. Häsing and B. Blümich, *Nature Physics* 2006, **2**, 10.
14. M.P. Ledbetter, T. Theis, J.W. Blanchard, H. Ring, P. Ganssle, S. Appelt, B. Blümich, A. Pines and D. Budker, *Phys. Rev. Lett.* 2011, **107**, 107601.
15. S. Appelt, F. W. Häsing, H. Kühn and B. Blümich, *Physical Review A* 2007, **76**, 23420.
16. J. Colell, P. Türschmann, S. Glöggler, P. Schleker, T. Theis, M. Ledbetter, D. Budker, A. Pines, B. Blümich and S. Appelt, *Phys. Rev. Lett.* 2013, **110**, 137602.
17. J. Natterer and J. Bargon, *Progress in Nuclear Magnetic Resonance Spectroscopy* 1997, **31**, 293.
18. S. Glöggler, J. Colell and S. Appelt, *J. Magn. Res.* 2013, **235**, 130.
19. S. Appelt, F. Häsing, H. Kühn, J. Perlo and B. Blümich, *Phys. Rev. Lett.* 2005, **94**, 197602.
20. T. Theis, P. J. Ganssle, G. Kervern, S. Knappe, J. Kitching, M. P. Ledbetter, D. Budker and A. Pines, *Nature Physics* 2011, **7**, 571.
21. M. C. Butler, G. Kervern, T. Theis, M. P. Ledbetter and P. J. Ganssle, *J. Chem. Phys.* 2013, **138**, 234201.
22. P. C. Maurer, G. Kucsko, C. Latta, L. Jiang, N. Y. Yao, S. D. Bennett, F. Pastawski, D. Hunger, N. Chisholm, M. Markham, D. J. Twitchen, J. I. Cirac and M. D. Lukin, *Science* 2012, **336**, 1283.
23. P. R. Vasos, A. Comment, R. Sarkar, P. Ahuja, J.-P. Ansermet, J. A. Konter, P. Hautle, B. van den Brandt and G. Bodenhausen, *Proc. Natl. Acad. Sci.* 2009, **106**, 18469.
24. M. Emondts, M.P. Ledbetter, S. Pustelny, T. Theis, B. Patton, J. W. Blanchard, M. C. Butler, D. Budker and A. Pines, *Phys. Rev. Lett.* 2014, **112**, 077601.
25. H. Günther, NMR Spectroscopy, John Wiley & Sons (New York, 1980).
26. M.H. Levitt, Spin Dynamics: Basics of Nuclear Magnetic Resonance. John Wiley & Sons (New York, 2008).
27. S. Appelt, F.W. Häsing, U. Sieling, A. Gordji-Nejad, S. Glöggler and B. Blümich, *Phys. Rev. A* 2011, **81**, 023420.
28. J. Natterer, O. Schedletzky, J. Barkemeyer, J. Bargon and S. G. Glaser, *J. Magn. Res.* 1998, **133**, 92.
29. K. L. Ivanov, A. V. Yurkovskaya and H.-M. Vieth, *Z. Phys. Chem.* 2012, **226**, 1315.
30. S. Aime, R. Gobetto, F. Reineri and D. Canet, , *J. Magn. Res.* 2006, **178**, 184.
31. S. Appelt, S. Glöggler, F. Häsing, U. Sieling, A. Gordji Nejad and B. Blümich, *Chem. Phys. Lett.* 2010, **485**, 217.
32. D. I. Hoult and R.E. Richards, *J. Magn. Res.* 1976, **24**, 71.
33. A. G. Webb, *Progress in Nuclear Magnetic Resonance Spectroscopy* 1997, **31**, 1.
34. S.R. Hartmann and E.L. Hahn, *Phys. Rev.* 1962, **128**, 2042.
35. G.A. Morris and R. Freeman, *J. Am. Chem. Soc.* 1979, **101**, 760.
36. M. Haake, J. Natterer and J. Bargon, *J. Am. Chem. Soc.* 1996, **118**, 8688.
37. C. Cai, A. M. Coffey, R. V. Shchepin, E. Y. Chekmenev and K. W. Waddell, *J. Phys. Chem. B* 2013, **117**, 1219.
38. J. Barkemeyer, M. Haake and J. Bargon, *J. Am. Chem. Soc.* 1995, **117**, 2927.
39. M. Haake, J. Natterer, J. Bargon, *J. Am. Chem. Soc.* 1996, **118**, 8688.

40. L.T. Kuhn, U. Bommerich and J. Bargon, *J. Phys. Chem. A* 2006, **110**, 3521.
41. A. Harthun, R. Giernoth, C. J. Elsevier and J. Bargon, *Chem. Commun.* 1996, **21**, 2483.
42. G. Pileio, M. Carravetta and M. H. Levitt, *Proc. Nat. Acad. Soc*. 2010, **107**, 17135.
43. H. Kalinowski, S. Berger and S. Braun 13C-NMR Spektroskopie, Georg Thieme Verlag, Stuttgart (1984).
44. L. Buljubasich, M. B. Franzoni, H. W. Spiess and K. Münnemann, *J. Magn. Reson.* 2012, **219**, 33.
45. M. Goldman, H. Jóhannesson, O. Axelsson and M. Karlsson, *C. R. Chimie* 2006, **9**, 357.
46. M. Carravetta, O. G. Johannessen and M. H. Levitt, *Phys. Rev. Lett.* 2004, **92**, 153003-1.